

Sub-Band-Gap Absorption Mechanisms Involving Oxygen Vacancies in Hydroxyapatite

Vladimir S. Bystrov,[†] Leon A. Avakyan,[‡] Ekaterina V. Paramonova,[†] and José Coutinho^{*,¶}

[†]*Institute of Mathematical Problems of Biology, Keldysh Institute of Applied Mathematics, Russian Academy of Sciences, Vitkevicha street 1, Pushchino, 142290, Moscow region, Russian Federation*

[‡]*Physics Faculty, Southern Federal University, Zorge street 5, Rostov-on-Don 344090, Russian Federation*

[¶]*Department of Physics & I3N, University of Aveiro, Campus Santiago, 3810-193 Aveiro, Portugal*

E-mail: jose.coutinho@ua.pt

Phone: +351 234 247051. Fax: +351 234 378197

Abstract

Hydroxyapatite (HAp) is a widely used biomaterial for the preparation of bone and dental implants. Despite the relevance of HAp in medicine, exciting applications involving this material as a bio-compatible photocatalyst, depend on how well we understand its fundamental properties. Experimental evidence suggests that oxygen vacancies play a critical role in the production of surface radicals upon exposure of HAp to ultra-violet (UV) light. However, very little is known about the underlying physical and chemical details. We present a hybrid density-functional study of the structural and electronic properties of oxygen vacancies in large HAp supercells within the plane-wave formalism. We find that under equilibrium conditions, vacancies occur either as a simple vacant oxygen site (in the neutral charge state), or as extended structures replacing several crystalline moieties (in the double plus charge state). Large atomic relaxations upon ionization make the oxygen vacancy a negative- U defect, where the single plus charge state is metastable, being only accessible under UV excitation. From inspection

of the transition levels, we find that electron promotion from the valence band top to the donor state of the vacancy, involves a zero-phonon transition of 3.6-3.9 eV. This mechanism is the most likely explanation to the 3.4-4.0 eV absorption onset for the observation of photocatalysis using HAp under persistent UV illumination. *Published in Journal of Physical Chemistry C*, **123**, 4856-4865 (2019). <https://doi.org/10.1021/acs.jpcc.8b11350>

Introduction

Hydroxyapatite (HAp) $[\text{Ca}_{10}(\text{PO}_4)_6(\text{OH})_2]$ is the main mineral component of bone tissue and teeth, along with the organic component (collagen) and living bone cells (osteoclasts, osteoblasts and osteocytes).¹⁻⁵ HAp crystallizes within the gaps of stacked tropocollagen fibrils, forming and strengthening the bone structure.⁴⁻⁷

Upon bone fracture/destruction, bone repair occurs through simultaneous formation of the organic base and crystallization of HAp in the form of platelets or needle-like nanocrystals.

tals.⁴⁻⁸ Such innate bio-activity and compatibility, makes HAp a widely used material in medicine, with applications in bone and dental implants, often integrating and covering other stiffer materials in order to meet specific mechanic requirements.⁹⁻¹¹

It is important to distinguish between mineral (stoichiometric) from biological HAp (bio-HAp) found in living organisms. The latter differs from the ideal crystal due to stoichiometric imbalances in the form of defects (*e.g.* oxygen vacancies, OH-group vacancies and interstitial protons) or even impurities, among which carbonate ions are the most relevant. The importance of defects is paramount — besides polarizing the surface of bio-HAp, which is critical for adhesion with living tissues and bone regeneration,¹²⁻¹⁵ defects are also responsible for several physical properties, promising exciting functionalities to HAp. For instance, due to its peculiar OH-channels, protons were suggested to travel long distances under the influence of electric fields, thus enabling the production of a “persistent polarization”.¹⁶⁻¹⁸

Tofail *et al.*¹⁹ interpreted the polarization of HAp as arising from a collective alignment of individual OH anions. Accordingly, an anti-ferroelectric to ferroelectric transition was found at 210 °C by monitoring the temperature dependence of the dielectric constant of HAp. Particularly elucidating experiments were described by Hitmi and co-workers^{20,21} regarding the flipping dynamics of OH⁻ anions in F⁻ or Cl⁻ heavily doped material. Accordingly, thermal stimulated current measurements were employed to monitor the polarization changes in the material as the temperature was progressively increased. Interestingly, they interpreted that the 210 °C phase change as an entangled flipping of OH-chains, which was hindered in doped material due to formation of F⁻ ··· H⁺O²⁻ or Cl⁻ ··· H⁺O²⁻ hydrogen bonds.

The collective interactions between OH dipoles confer to HAp properties like ferroelectricity, pyroelectricity and piezoelectricity,²²⁻²⁴ making HAp a strong contender for charge storage applications²⁵ as well as to fabricate bio-electronic devices for *in-vivo* and *ex-vivo*

applications.²⁶

Another feature exhibited by HAp is the capability of degrading hazardous organic and inorganic chemicals, both in air and water, upon exposure to ultra-violet (UV) light.²⁷⁻³⁴ In fact, HAp was demonstrated to rival against powerful and well-established photo-catalysts such as TiO₂. However, unlike the latter, HAp has the advantage of showing strong affinity for organic compounds and living organisms, bringing obvious advantages for instance if used for environmental remediation or cancer treatment.³⁵⁻³⁷ Again, defects and dopants play a central role here. Electron spin resonance (ESR) studies clearly show that the surface reactive species is superoxide O₂^{•-}.^{27,38} This radical is formed when adsorbed oxygen captures an UV-excited electron from a defect, most probably an oxygen vacancy.^{27,38} The photocatalytic activity of HAp seems to be thermally controllable — heat treatments around 200 °C resulted in efficient photo-degradation of several pollutants, while treating the same powder at 1150 °C led to photo-inactive material.²⁷ This effect was correlated with the detection of O₂^{•-} and OH[•] radicals by ESR.³⁹ It is not clear why annealing at a moderate temperature results in photo-active HAp, whereas high-temperature treatments deactivates photocatalysis. It is known that high temperature treatments improve crystallinity but also result in the loss of OH⁻ anions. Given the above annealing temperatures, it is tempting to relate the activation of the photocatalytic activity after 200 °C heat treatments, with the motion/polarization of OH-anions (also taking place at about this temperature¹⁹). Unfortunately, the available data in the literature is too scarce to draw any definite conclusion. Further experiments would be important to clarify this aspect, for instance by simultaneously monitoring the crystalline structure and photo-catalysis activity of samples after being subject to different thermal treatments.

In a latter report, using X-ray photoemission (XPS) and Fourier-transform infra-red (FTIR) spectroscopy, Nishikawa³⁸ found that the low-temperature annealed material (200 °C) showed some changes in the phosphate groups upon UV illumination, suggesting that a perturbation of

P-O bonds were connected to the production of $\text{O}_2^{\bullet-}$ surface radicals. A drastic decrease in the intensity of several absorption bands related to P-O vibrations was actually observed after exposing as-grown HAp samples to UV light for 1 hour.^{30,32} The IR spectrum regained its original shape after leaving a used HAp sample in darkness for 1 hour, demonstrating that the UV-induced transformation of the P-O bonds was reversible.³⁰

An important question is therefore: what are the details of the physical and chemical mechanisms behind these photo-catalytic processes? It is clear that oxygen vacancies and related defects play a crucial but yet unknown role, which will stay undisclosed while their electronic and optical properties are largely unexplored.

Recently, several point defects in HAp were inspected by means of local density density functional theory, where it was found that an oxygen vacancy in the phosphate (PO_4) unit introduces a fully occupied state in the lower half of the gap.⁴⁰ The photoionization of this level was actually claimed to account for the photocatalytic threshold in the range 3.4-4.0 eV.⁴¹ However, the lack of physical significance of the Kohn-Sham eigenvalues, along with large self-interaction errors from the local density approximation, make any assignment of optical data a highly speculative exercise.⁴²

In order to obtain an accurate picture of the electronic and optical properties of defects in a material like HAp, it is crucial to accurately describe the physics of the material itself, which includes properties such as the crystalline structure, the electronic band structure, dielectric response, among others.

In a recent work, we have shown how the quality of the exchange-correlation treatment affects the above properties.⁴³ We found out that the use of hybrid density functional theory (hybrid-DFT), which mixes a portion of Fock exchange with a (semi-)local exchange-correlation potential, leads to electronic properties very close to those obtained using highly accurate many-body perturbation theory within the *GW* framework. While the *GW* and hybrid-DFT band gaps were close to 7 eV, generalized gradient approximated results underesti-

mated this figure by 30%.^{40,44-48} Comparable errors are therefore expected for the calculated electronic and optical properties of defects, as shown for the case of the OH vacancy in HAp.⁴³ From the experimental perspective, measurements of the band gap width of HAp have been controversial. Whereas combined photoluminescence and surface photovoltage spectroscopy studies found a band gap approaching 4 eV,⁴⁹ diffuse reflectance spectra in the UV-VIS region indicate that the gap should be wider than 6 eV,³¹ thus confirming the *GW* results.⁴³ We can only explain the narrower photoluminescent gap with the presence of defects with levels close to mid-gap. Further, we know that (semi-)local DFT severely underestimates the band gap width of semiconductors and insulators. A typical generalized gradient approximated calculation gives $E_g = 5.2$ eV (see Ref. 43 and references therein), making the reported gap of 4 eV unrealistic.

In view of the above, we present below a theoretical study of the electronic properties of oxygen vacancies in HAp, which allows us to connect their structure stability, charge state transitions and photoionization energies with the optical excitation needed for the observation of efficient photocatalytic activity.

Methods

The calculations were carried out using density functional theory (DFT), as implemented by the Vienna Ab-initio Simulation Package (VASP).⁵⁰⁻⁵² The exchange-correlation potential was evaluated either using the generalized gradient approximation according to Perdew, Burke and Ernzerhof (PBE),⁵³ or the Becke three-parameter, Lee-Yang-Parr (B3LYP) hybrid functional,^{54,55} which incorporates a fraction of exact exchange with local and semi-local functionals. Due to severe limitations of the (semi-)local functionals alone in describing the electronic structure of HAp near the band gap,⁴³ the use of hybrid-DFT turns out to be critical in the calculation of the vacancy transition levels. Core states were described by means of the projector augmented wave (PAW)

method,⁵⁶ while the Kohn-Sham problem was addressed by using plane-waves with kinetic energy up to $E_{\text{cut}} = 400$ eV to expand the wave functions. For further details, including convergence tests, we direct the reader to Ref. 43.

Oxygen vacancies were introduced in hexagonal supercells made up of $2 \times 2 \times 2 = 8$ polar HAp unitcells (spacegroup $P6_3$ and #173 in the crystallographic tables), comprising a total of 352 atoms. Although the monoclinic phase $P2_1/b$ was found to be more stable,^{57,58} they only differ by a few tens of meV per unit cell, with their electronic structures being essentially identical⁴⁸. The equilibrium lattice parameters of $P6_3$ -symmetric HAp were $a = 9.537$ Å and $c = 6.909$ Å ($a = 9.577$ Å and $c = 6.877$ Å) as obtained within PBE (B3LYP) level calculations. These compare well with the experimental figures $a = 9.417$ Å and $c = 6.875$ Å.⁵⁹ A full relaxation of such large supercells using plane-wave hybrid-DFT is prohibitively expensive. Instead, defect structures were first found by relaxing all atomic coordinates within PBE, until the maximum force became less than 10 meV/Å. The resulting structures were employed on a second step, where the total energy was obtained within hybrid-DFT by means of a single-point calculation. This procedure was necessary due to the sheer size of the Hamiltonian at hand combined with the use of a plane-wave method. We have recently shown that relative energies obtained within this methodology are usually affected by error bars of the order of 10 meV or lower.^{60,61} For instance, the energy difference between HAp unit cells with $P6_3$ and $P6_3/m$ symmetry (the latter being obtained by aligning the OH units along opposite directions) is $E(P6_3/m) - E(P6_3) = 0.39$ eV with both energies being obtained from fully relaxed B3LYP-level calculations. An analogous quantity obtained from energies calculated according to the two-step recipe described above, differed by less than 5 meV from this figure. We also calculated the energy difference between oxygen vacancies of type I and IV (see beginning of Section). For practical reasons, these calculations were carried out by placing the defects in single unit cells. While fully relaxed B3LYP-level calculations give 1.37 eV (in favor

of the O(IV) vacancy), the B3LYP single-point calculation (using the PBE-relaxed structure) gives 1.31 eV, also favoring the O(IV) vacancy.

For the HAp unit cell, we have shown previously that convergence of the electron density and energy is obtained when sampling the band structure with a Γ -centered $2 \times 2 \times 3$ mesh of \mathbf{k} -points within the first Brillouin zone (BZ). By doubling the size of the cell along all principal directions, reciprocal lattice vectors are contracted by a factor of two, so that a $1 \times 1 \times 2$ \mathbf{k} -point grid would actually improve on the sampling quality. From convergence tests, we found that the total energy of the 352-atom bulk supercell obtained with a $1 \times 1 \times 1$ grid (Γ -point sampling) differs by less than 0.1 eV from a $1 \times 1 \times 2$ -sampled calculation. More importantly, relative energies and ionization energies of defects differ by about 1 meV only. Therefore, all defect calculations employed a Γ -point sampling.

The formation energy of a defect in a crystalline sample (with arbitrary volume) can be written as,⁶²

$$E_f = E(q, R) - E_{\text{HAp}} - \sum_i \Delta n_i \mu_i + q(E_v + E_F), \quad (1)$$

which depends primarily on the energy difference between defective and pristine crystals, namely E and E_{HAp} , respectively. The defect is considered on a particular configuration R and charge state q . The third and fourth terms account for any stoichiometric and charge imbalances between the first two terms. Accordingly, μ_i are chemical potentials for any species i which are respectively added ($\Delta n_i > 0$) or removed ($\Delta n_i < 0$) from or to the perfect crystal to make the defect. The last term accounts for the energy involved in the exchange of electrons between the defect in charge state q and an *electron reservoir* with a chemical potential $\mu_e = E_v + E_F$, where E_v and E_F stand for the energy of the valence band top and Fermi level, respectively. The latter mostly depends on the type and amount of defects and impurities in the crystal, and can vary in the range $0 \leq E_F \leq E_g$, where E_g is the band gap width

of the material.

For an oxygen vacancy, $\Delta n_{\text{O}} = -1$ and $\Delta n_i = 0$ otherwise, so that the third term in Eq. 1 reduces to the oxygen chemical potential (μ_{O}). In the present work we are mainly interested in the electronic properties of the oxygen vacancy, which are independent of the choice of the chemical potentials. Hence, we simply consider μ_{O} as the energy per atom in molecular oxygen. This was calculated by placing a molecule in a box (edge length 20 Å) in the spin-1 ground state.

Finally, we note that because we are using periodic boundary conditions, the calculation of a defect with net charge q within the supercell would lead to a diverging total energy. This is avoided by spreading a uniform background counter-charge with density $\rho_{\text{back}} = -q/\Omega$ over the cell volume Ω .⁶³ The spurious Coulomb interactions between the periodic array of charged defects and background must be removed from the periodic total energy \tilde{E} , so that the energy of the defective crystal in Eq. 1 should be replaced by $E = \tilde{E} + E_{\text{corr}}$, where the correction term E_{corr} was obtained according to the method proposed by Freysoldt, Neugebauer and Van de Walle⁶⁴, and recently generalized for anisotropic materials.⁶⁵

Results

Crystalline HAp has oxygen atoms on four symmetry-inequivalent sites, which are referred to as oxygen types I-IV. Types I, II and III are in the phosphate units, while type IV oxygen atoms are located in the OH^- anions. These are denoted as O(I),...,O(IV) and are shown in the upper half of Figure 1, where portions of bulk HAp are depicted. We note that PO_4 groups have two nearly symmetric O(III) atoms which are superimposed in the upper view of bulk HAp in Figure 1.

Before describing the structure of the oxygen vacancies it is convenient to leave a few words about notation. An oxygen vacancy in charge state q is denoted as $\text{V}_{\text{O}(R)}^q$, where R stands for a particular structure label. It is important to understand that q is the net charge of the whole

defect (enclosing its core and possibly many ligands) and must be distinguished from the oxidation state of the moieties that make the core of the defect. Access to such information would be provided with a description of the electronic state of the defect, preferably using a compact recipe. For instance, the creation of a neutral oxygen vacancy in the HAp lattice can be described as a replacement of a PO_4^{3-} moiety in pristine HAp by a PO_3^{3-} anion, both in the -3 oxidation state, thus ensuring charge neutrality of the whole sample. Along these lines, we introduce a more informative defect notation, namely $[\text{X}^n]_Y^q$, which represents a defect moiety X in oxidation state n , replacing a crystalline site/moiety Y with oxidation state $m = n - q$, thus leading to a defect with net charge q . For instance, a positively charged oxygen vacancy can either be referred to as V_{O}^+ or alternatively as a PO_3^{2-} anion replacing a PO_4^{3-} moiety, *i.e.*, $[\text{PO}_3^{2-}]_{\text{PO}_4}^+$.

Among the many vacancy structures investigated, those shown in Figures 1(a)-(e) are the most relevant as they showed lower energy. Metastable structures with more than 2 eV above the ground state (for each particular charge state) will not be discussed. Figure 1(a) describes the formation of a pyramidal PO_3 structure, where removal of the O(I) atom in “Bulk HAp” highlighted using a bright red color, leads to $\text{V}_{\text{O(I)}}$ as shown in the lower part of the figure, where a “Defective HAp” region is shown. Analogous structures for $\text{V}_{\text{O(II)}}$ and $\text{V}_{\text{O(III)}}$ were obtained as well. In the neutral charge state the resulting $[\text{PO}_3^{3-}]_{\text{PO}_4}^0$ structures display a fully occupied sp^3 orbital on the P atom, resembling the phosphine molecule. This is shown in Figure 2(a), where an isosurface of the electron density corresponding to the highest occupied state is represented in blue for the specific case of $\text{V}_{\text{O(III)}}^0$. Figure 1(b) shows the case of a missing O(IV) atom, leaving an isolated H atom in the OH channel. This defect can be rationalized as the removal of neutral O from OH^- , leaving an hydride anion to maintaining charge neutrality of the whole system. In the neutral charge state we have a $[\text{H}^-]_{\text{OH}}^0$ structure, where after structural relaxation the hydride species becomes located close to the

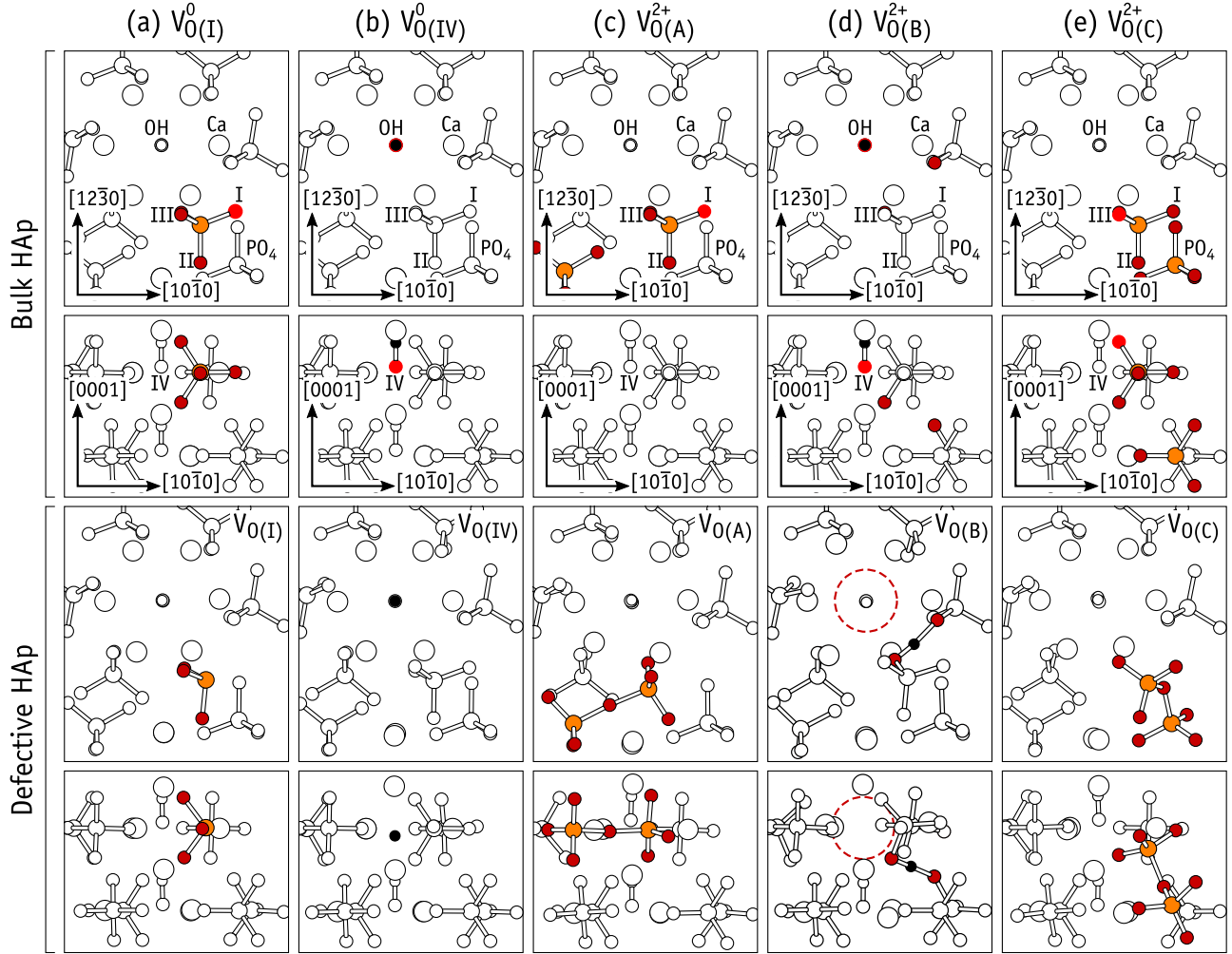


Figure 1: Atomistic diagrams showing “Bulk” (upper half) and “Defective” (lower half) HAp. For each row pair, upper and lower rows display the same structures viewed along $[0001]$ and $[12\bar{3}0]$ directions of the hexagonal lattice, respectively. Formation of structures I, IV, A, B and C of V_O defects is explained in columns (a)-(e). Only atoms belonging to the core of the defect are colored (P, O and H atoms are shown in orange, red and black, respectively). Vacancies were created by removing the bright-red O-atom shown in the “Bulk” figures. Upon atomic relaxation, the resulting structures are those in the corresponding “Defective” figures.

site of the missing O(IV) atom (compare lower diagrams of bulk and defective HAp in Figure 1(b)). The density corresponding to the highest occupied state of $V_{O(IV)}^0$ is represented in 2(b), which clearly shows the formation of an hydride anion in the OH-channel.

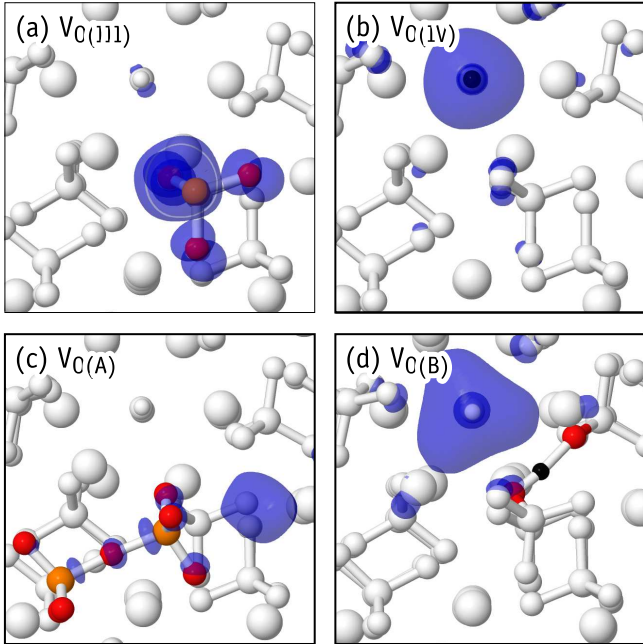


Figure 2: Electron density isosurfaces from the highest occupied Kohn-Sham level of neutral V_O defects in HAp. The density of $V_{O(III)}$ in (a) is representative of $V_{O(I)}$ and $V_{O(II)}$ as well. Isosurfaces are drawn at constant electron density $n = 0.001 \text{ \AA}^{-3}$.

In $V_{O(I)}-V_{O(IV)}$ defects, all atoms (but the missing oxygen) remain essentially close to their original crystalline coordinates, hence the use of subscripted O(I)-O(IV) labels to identify their structure. However, additional structures, hereafter referred to as *extended* structures, were also found for the oxygen vacancy in HAp. One type of such extended structures can be described as a pair of neighboring oxygen vacancies connected by an O-interstitial, $2V_O + O$. A second type is best described as a complex made of an OH-vacancy next to an H-interstitial, $V_{OH} + H$. Two defects of type $2V_O + O$ are singled out and labeled $V_{O(A)}$ and $V_{O(C)}$. They are shown in Figures 1(c) and 1(e). One $V_{OH} + H$ defect is shown in Figure 1(d) and is referred to as $V_{O(B)}$. A dashed circle is used in the figure to highlight the missing OH unit. The

highest occupied state of the extended structures is shown in Figures 2(c) and 2(d). They either overlap void regions of the HAp crystal or the vacant volume of the OH-channel, thus suggesting that they are donors with anti-bonding character or strong resonance with conduction band states.⁴³

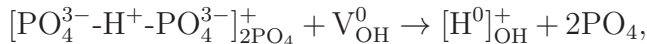
We found that the structure and stability of V_O defects strongly depend on the charge state. For neutral and single positive vacancies, only $V_{O(I)}-V_{O(IV)}$ are stable. In these charge states, extended configurations ($V_{O(A)}-V_{O(C)}$) relax to a $V_{O(I)}-V_{O(IV)}$ structure. Conversely, for charge state +2, structures $V_{O(I)}-V_{O(IV)}$ are unstable and relax to an extended configuration.

For relaxations in charge state +2 that started from structures I and III the final structures were respectively A and C. Here, the P atom of the PO_3 unit in $V_{O(I)}$ (or $V_{O(III)}$) moved across the plane defined by the three O atoms to connect to the O atom from the nearest PO_4 moiety. Such a severe relaxation can be explained by electron transfer from a neighboring PO_4^{3-} anion to the empty $P(sp^3)$ orbital of $[PO_3]_{PO_4}^{2+}$ in $V_{O(I)}^{2+}$ or $V_{O(III)}^{2+}$ (see Figure 2(a)), and the subsequent formation a new P-O bond. The result is an extended $[PO_3^{2-}-O-PO_3^{2-}]_{2(PO_4)}^{2+}$ structure shown in Figures 1(c) and 1(e).

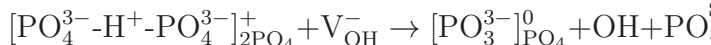
When initiating the relaxation in charge state +2 from structures II and IV, the resulting configuration was in both cases $V_{O(B)}^{2+}$. In this charge state, the defect comprises an interstitial H^+ next to a positively charged OH-vacancy, *i.e.*, $[PO_4^{3-}-H^+-PO_4^{3-}]_{2PO_4}^+ + V_{OH}^+$. The proton is located on a high electron density site between two oxygen anions. The net positive charge of the OH-vacancy follows from depletion of two electrons from the channel-state represented by the isosurface of Figure 2(d). When starting from structure II, Coulomb attraction and subsequent reaction between neighboring OH^- and $[PO_3]_{PO_4}^{2+}$ leads to the formation of the $V_{O(B)}^{2+}$ extended structure. Alternatively, when starting from structure IV, a proton in the initial $[H^+]_{OH}^{2+}$ configuration is strongly attracted by O-anions in neighboring PO_4^{3-} moieties, also ending up in $V_{O(B)}^{2+}$ as depicted in Figure 1(d).

Upon relaxation of neutral and positively charged structures A and C, the final defect

configurations were I and III, respectively. For neutral and positively charged relaxations of structure B, the resulting structure depends on the charge state. When starting from $V_{O(B)}^+$, the V_{OH} state of Figure 2(d) is partially occupied. The O-H⁺-O unit dissociates spontaneously, with the proton jumping into the OH channel to overlap with the V_{OH} electron and form neutral hydrogen,



ending up in the $V_{O(IV)}^+$ state. Conversely, when starting from $V_{O(B)}^0$, the state shown in Figure 2(d) becomes fully occupied, so that the OH-vacancy is negatively charged. During atomic relaxation, an (OH)⁺ unit breaks away from the O-H⁺-O structure to fill in the nearby OH-vacant site. The mechanism is therefore



now ending up in the $V_{O(II)}^0$ state.

Relative defect energies in all charge states of interest are reported in Table 1, which includes both PBE- and B3LYP-level results. It is interesting to note that within the same charge state, both PBE and B3LYP data display quite a consistent picture, with relative energies differing by less than 0.2 eV. However, as we will show below, that is not the case when we compare electronic transition energies obtained using the semi-local and hybrid density functionals.

In broad terms, Table 1 shows that neutral $V_{O(IV)}^0$ in HAp is a distinct ground state. Pyramidal $V_{O(I)}^0$ - $V_{O(III)}^0$ defects are at least 1 eV higher in the energy scale. Single positively charged V_O^+ is most stable when adopting the pyramidal structure III. Other competing states with analogous configurations (I and II) are metastable by about 0.3 eV. For the double plus V_O^{2+} defect, the ground state is structure C (see Figure 1(e)). The distance between the interplanar phosphorous atoms in bulk HAp is 4.1 Å, which is shorter than the intra-planar P...P distance (4.8 Å). The shorter inter-planar distance favors the formation of $V_{O(C)}^{2+}$ (in detri-

ment of $V_{O(A)}^{2+}$) by conferring some p-character to the lone states of the bridging O atom, and making $V_{O(A)}^{2+}$ metastable by at least 1.3 eV. This is evident in Figures 1(c) and 1(e), that show P-O-P angles of 175° and 125°, respectively. Finally, we found a competing double positive state, namely structure B, only 0.2 eV above the ground state. As described in Figure 1(d), structure B comprises an OH vacancy next to H interstitial. Interestingly, the energy of infinitely separated V_{OH}^+ and H⁺ defects (obtained from independent supercell calculations) is 0.2 eV lower than that of $V_{O(B)}^{++}$, being essentially degenerate to $V_{O(C)}^{++}$. In these calculations, the isolated proton was found to be more stable when located between two O(III) atoms, forming a O-H-O structure with slightly asymmetric OH distances (analogously to Figure 1(d)).

Although further work is necessary, we may speculate that once a $V_{O(B)}^{++}$ defect is formed, the separation of V_{OH}^+ and H⁺ is most likely to take place via consecutive jumps of neighboring OH⁻ anions into the positively charged OH-vacancy.

Defect structures described above were only investigated in neutral, positive and double positive charge states. Inspection of the Kohn-Sham eigenvalues at $\mathbf{k} = \Gamma$ confirmed that V_O defects are all donors. The diagram in Figure 3 shows the B3LYP Kohn-Sham energies of neutral vacancies in the energy range of the one-electron band gap $\epsilon_{cb} - \epsilon_{vb} = 7.34$ eV. Here ϵ_{cb} and ϵ_{vb} are energies of the bottom and top of the conduction band and valence band, respectively. These are represented by solid horizontal lines spanning the whole diagram width. Short horizontal lines represent the defect-related states, as obtained from the Kohn-Sham eigenvalues. Level occupation is indicated by upward and downward arrows. The value of ϵ_{cb} was chosen to be at the origin of the energy scale. We note that since structures A-C are only stable in the double plus charge state, their one electron energies were obtained from neutral single-point calculations using $V_{O(A)}^{2+}$ - $V_{O(C)}^{2+}$ atomic structures.

The electronic structure of $V_{O(II)}$ and $V_{O(III)}$

Table 1: Relative energies of V_O defects in HAp with respect to the lowest energy structure in a particular charge state (highlighted in bold). Results from both PBE and B3LYP calculations are reported. For unstable structures, the energy is replaced by the label of the respective structure obtained after relaxation. All values are in eV.

Structure	Functional	V_O^0	V_O^+	V_O^{++}
I	PBE	1.01	0.33	A
	B3LYP	1.17	0.35	
II	PBE	0.96	0.23	B
	B3LYP	1.14	0.34	
III	PBE	0.88	0.00	C
	B3LYP	1.03	0.00	
IV	PBE	0.00	0.67	B
	B3LYP	0.00	0.54	
A	PBE	I	I	1.21
	B3LYP			1.35
B	PBE	II	IV	0.17
	B3LYP			0.19
C	PBE	III	III	0.00
	B3LYP			0.00

were essentially identical to that of $V_{O(I)}$. Considering that all diagrams refer to neutral states, it becomes evident that V_O defects show no empty gap states, and therefore cannot trap electrons. Hence, V_O defects in HAp are not stable in the negative charge state.

Although the Kohn-Sham band structure lacks physical significance, we can always make use of Koopmans' theorem to connect the highest occupied state to the photo-ionization energy of the system under scrutiny.^{66,67} With this in mind, it is evident that the simpler $V_{O(I)}$ - $V_{O(IV)}$ structures are deep donors with photo-ionization energies close to 6 eV, while semi-vacancy configurations are shallower donors, where promotion of electrons to the conduction band requires a low ionization energy. This makes $V_{O(A)}^{2+}$, $V_{O(B)}^{2+}$ and $V_{O(C)}^{2+}$ rather stable species.

The energy of the highest occupied states in Figure 3 account for *vertical* transitions which are in principle accessible by optical excitation. However, transition levels (or electronic levels) of defects are equilibrium properties and must

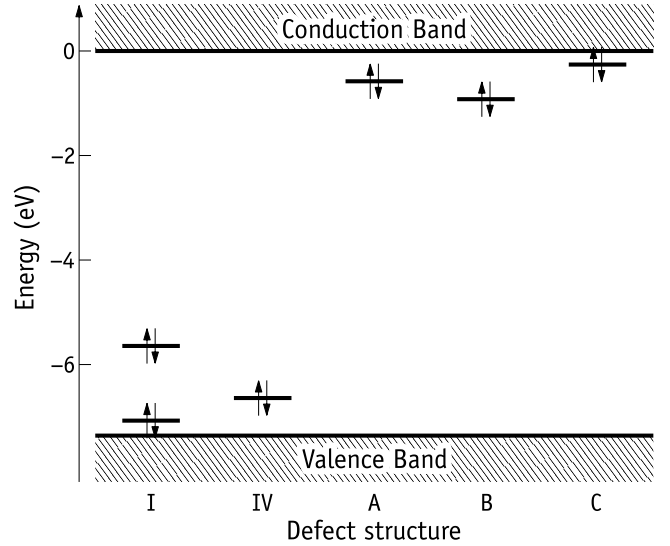


Figure 3: Kohn-Sham energy levels of neutral V_O defects in a HAp supercell at the $\mathbf{k} = \Gamma$ point. Defect structure I is also representative of structures II and III (see text). The latter have gap states that deviate from those of $V_{O(I)}$ by less than 0.2 eV.

be derived from the formation energy of both ground states involved in the transitions. This is analogous to the zero-phonon (ZP) line energy in photoluminescence/absorption experiments. Hence, the energy of a transition level of a defect will differ from the vertical (optical) transition by a Franck-Condon relaxation energy. These issues will be discussed below.

Equation 1 allows us to construct a *phase diagram* for the oxygen vacancy in HAp as a function of the chemical potentials and Fermi energy. This is particularly useful for defects which adopt different structures in several charge states, allowing us to immediately identify the most stable states for a particular position of the Fermi energy. The value of E_F for which two solutions $E_f(q)$ and $E_f(q+1)$ from Eq. 1 become identical, defines a threshold above which V_O^q is more stable than V_O^{q+1} . This is the defect transition level and can be calculated with respect to the valence band top as,

$$E(q/q+1) - E_v = [E(q, R^q) - E(q+1, R^{q+1})] - I_{\text{bulk}}, \quad (2)$$

where we distinguish any possible different

structures R^q and R^{q+1} for charge states q and $q + 1$, respectively, E is the total energy (*cf.* Eq. 1), which incorporates a periodic charge correction for $q \neq 0$, and $I_{\text{bulk}} = E_{\text{bulk}}(q = +1) - E_{\text{bulk}}(q = 0)$ is the ionization energy of a bulk supercell. Note that alternatively, one could have replaced I_{bulk} in Eq. 2 by the energy of the highest occupied Kohn-Sham level from a bulk calculation. We have chosen to avoid the use of Kohn-Sham energies, keeping the results solely based on total energies. The Kohn-Sham band gap from B3LYP-level calculations ($E_{\text{g}}^{\text{KS}} = 7.34$ eV) is about 0.49 eV wider than the quasi-particle gap (calculated as $E_{\text{g}}^{\text{QP}} = E_{\text{bulk}}(+1) + E_{\text{bulk}}(-1) - 2E_{\text{bulk}}(0) = 6.85$ eV).

Figure 4 plots the formation energy for several V_{O} defects in different charge states according to Eq. 1. The horizontal axis represents the Fermi energy with $E_{\text{F}} = 0$ eV representing the valence band top and $E_{\text{F}} = 6.85$ eV the conduction band bottom. Horizontal, single positive and double positive sloped lines represent formation energies of V_{O}^0 , V_{O}^+ and V_{O}^{2+} , respectively. Solid lines stand for structures I-IV (in charge states $q = 0$ and $q = +1$), while dashed lines denote extended structures A, B and C (see legend). Thick lines highlight the lowest energy states, namely $V_{\text{O(IV)}}^0$ and $V_{\text{O(III)}}^{2+}$, for any position of E_{F} .

In line with the discussion above, among the formation energies of neutral defects (horizontal lines), that of $V_{\text{O(IV)}}^0$ is lowest, with other structures being metastable by about 1 eV. For the positive charge state, pyramidal $[\text{PO}_3^{2-}]_{\text{PO}_4}^+$ defects are more stable. In this case, structure III has lower energy, but structures I and II are metastable by only 0.35 eV. For double positively charged structures, $V_{\text{O(B)}}^{2+}$ and $V_{\text{O(C)}}^{2+}$ are the most stable, with a slight preference for $V_{\text{O(C)}}^{2+}$.

It is important to realize that under no circumstance the positive charge states are thermodynamically stable (irrespective of the Fermi energy location). Formation energies of V_{O}^+ defects are always higher than those of neutral and double positive defects. This property is usually referred to as negative- U ,^{68,69} alluding to the negative correlation energy between three consecutive charge states. This

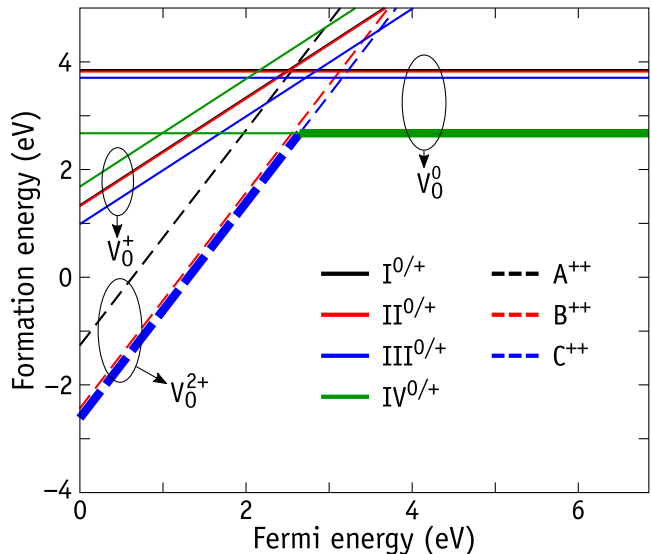


Figure 4: Formation energy diagram of the V_{O} defect in HAp as a function of the Fermi energy. Solid lines represent formation energies of neutral and single positive defects with structures I-IV, while dashed lines represent double positive defects with structures A-C.

is best illustrated if compared to the case of isolated atoms — here the n -th ionization energy (I_n) is smaller than the $(n + 1)$ -th ionization energy (I_{n+1}), where the correlation between the first ionized state and remaining electrons is $U = I_{n+1} - I_n > 0$. This is mostly due a decrease of electron-electron repulsion upon ionization (and a corresponding increase of electron-nuclei Coulomb attraction due to lower electronic screening). However, for some defects in crystals, as well as for some molecules, the first ionization leads to a strong atomic relaxation/transformation (not possible in single atoms), allowing a trade between the energy from bond formation/breaking, and the Coulomb energy which binds the ionized state. For sufficiently large relaxations, the second ionization energy may actually become smaller than the first, and the defect may effectively show a negative- U .

A consequence of a negative- U ordering of donor levels (as depicted in Figure 4), is an entangled promotion of two electrons to the conduction band when a neutral V_{O}^0 defect is excited by means of optical or thermal excitations. Analogously, when the defect is fully ion-

ized and there are free electrons available in the conduction band (upon exposure to ultra-violet light), the capture of the first electron (into V_{O}^+) will make the defect even more *eager* for a second capture (into V_{O}^0).

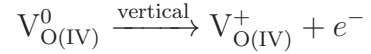
Another important feature is the fact that under thermal equilibrium, single positive defects are not stable. Considering the lowest energy structures for each charge state, namely $V_{\text{O(IV)}}^0$, $V_{\text{O(III)}}^+$ and $V_{\text{O(III)}}^{2+}$, we always have $E_{\text{f}}(2+) + E_{\text{f}}(0) < 2E_{\text{f}}(+)$, and only $V_{\text{O(IV)}}^0$ and $V_{\text{O(C)}}^{2+}$ (and/or possibly $V_{\text{O(B)}}^{2+}$) may occur. These states are represented by thick lines in Figure 4. It is clear that they define a (0/2+) transition level at the crossing point. The location of the level is calculated at $E(0/2+) - E_{\text{v}} = 2.65$ eV. Hence, for p-type HAp, where the Fermi energy is at the lower-half of the gap, oxygen vacancies are likely to adopt double positive extended structures $V_{\text{O(B)}}^{2+}$ or $V_{\text{O(C)}}^{2+}$. Conversely, in n-type (and intrinsic) HAp the neutral state is more stable and the defect will be found as an isolated H^- hydride in the OH-channel (*i.e.*, $V_{\text{O(IV)}}^0$).

For the sake of reference, we leave the reader with Table 2, where the calculated transition levels, $\Delta E(q/q+1) = E(q/q+1) - E_{\text{v}}$ involving the relevant structures R^q and R^{q+1} , can be found. Results based on both PBE and B3LYP functionals are reported. Unlike the energy differences in the same charge state (*c.f.* Table 1), it is evident that PBE results have error bars of at least 1 eV, which is in line with our findings reported in Ref. 43.

Discussion

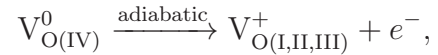
Our results suggest that under UV illumination, the most likely excitation channels for the oxygen vacancy are (i) electron emission from $V_{\text{O(IV)}}^0$ to the conduction band, (ii) hole-emission from $V_{\text{O(B)}}^{2+}$ or $V_{\text{O(C)}}^{2+}$ to the valence band (which is equivalent to the promotion of an electron from the valence band to the empty donor state of a double positive vacancy), or even (iii) electron emission from metastable $V_{\text{O(I)}}^0$ - $V_{\text{O(III)}}^0$ defects.

For the first case, the energy needed to perform a vertical transition from the ground state structure,



is estimated to be higher than $E_{\text{ph}} \sim 6.5$ eV (see Kohn-Sham levels for structure IV in Figure 3), where e^- represents an electron at the conduction band bottom. This energy is far too large to be connected with the optical excitation threshold observed during photocatalysis in the range 3.4-4.0 eV.⁴¹

As previously referred, the calculated electronic levels of Table 2 provide us access to zero-phonon (adiabatic) transition energies. For a neutral vacancy, adiabatic electron emission (ionization) energies are given by $E_{\text{ad}} = E_{\text{g}} - \Delta E(0/+)$. Hence, the lowest energy transitions in absorption follow



corresponding to an absorption energy $E_{\text{ad}} = 5.51$ eV, 5.49 eV, 5.16 eV for transitions where the final structures are $V_{\text{O(I)}}^+$, $V_{\text{O(II)}}^+$, and $V_{\text{O(III)}}^+$, respectively. In the above, $\Delta E(0/+) = 1.34$ eV, 1.36 eV and 1.69 are donor transition energies considering $R^0 = \text{IV}$ and $R^+ = \text{I, II and III}$, respectively, while $E_{\text{g}} = 6.85$ eV is the calculated quasi-particle gap width. Although the adiabatic transition energies are closer to the experimental data, kinetic effects are expected limit the exchange of oxygen between neighboring PO_4 and OH moieties,



where the first reactant and second product represent $V_{\text{O(IV)}}^0$ and $V_{\text{O(I,II,III)}}^+$ defects, respectively.

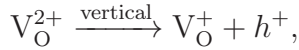
We also note that being a negative- U defect, under persistent excitation a second ionization of $V_{\text{O(I,II,III)}}^+$ would immediately follow the first, but now with considerably lower energy, *i.e.* in the range 3.3-4.3 eV, leading to the formation of $V_{\text{O(A,B,C)}}^{2+}$ defects.

Mechanism (ii), namely a hole-emission from $V_{\text{O(C)}}^{2+}$ or from $V_{\text{O(B)}}^{2+}$, would be likely in p-type

Table 2: Calculated electronic donor levels of V_O in HAp with respect to the valence band top, $\Delta E(q/q+1) = E(q/q+1) - E_v$. Both semi-local DFT (PBE) and hybrid-DFT (B3LYP) results are reported. Also indicated are defect structures, R^q , corresponding to each charge state in the transition. All values are in eV.

Functional	$\Delta E(0/+)$	R^0/R^+	$\Delta E(+/2+)$	R^+/R^{2+}
PBE	1.53	I/I	1.71	I/A
B3LYP	2.51		2.60	
PBE	1.58	II/II	2.64	II/B
B3LYP	2.50		3.74	
PBE	1.72	III/III	2.59	III/C
B3LYP	2.72		3.60	
PBE	0.17	IV/IV	3.08	IV/B
B3LYP	0.99		3.94	

HAp, where the Fermi energy is in the lower half of the band gap and the ground state is double positive (see Figure 4). Vertical transitions for both B and C structures follow



where h^+ stands for a hole in the valence band, and the energy as estimated from the B3LYP one-electron energies is close to 7 eV. Such a large value results from the shallow donor nature of the extended defects, which place the donor transition very high in the gap (see Figure 3).

If we instead consider an adiabatic hole emission from $V_{O(C)}^{2+}$ to the lowest energy V_O^+ structure, *i.e.* $V_{O(III)}^+$, we find 3.6 eV, in rather good agreement with the optical experiments.⁴¹ This mechanism involves a transition between ground states (in their respective charge state), consisting on breaking one of the P-O bonds in the $O_3P-O-PO_3$ extended structure of $V_{O(C)}^{2+}$.

The adiabatic transition from $V_{O(B)}^{2+}$ to $V_{O(II)}^+$ involves an absorption of 3.7 eV, but in this case the mechanism implies the a displacement of OH^- from the $V_{O(B)}^{2+}$ structure (see Figures 1(e)) to the OH-channel of the HAp lattice. Alternatively, a transition from $V_{O(B)}^{2+}$ to $V_{O(IV)}^+$ simply involves a jump of H from the O-H-O unit in $V_{O(B)}^{2+}$ to a close OH site in $V_{O(IV)}^+$,



which we find to proceed spontaneously (without an impeding barrier) upon hole emission. In the transition above, the reactants and first product represent $V_{O(B)}^{2+}$ and $V_{O(IV)}^+$ defects, respectively. The energy needed for the transformation is 3.9 eV, also accounting well for the observed UV absorption energy.

Finally, considering (iii) the photo-ionization of metastable neutral $V_{O(I)}-V_{O(III)}$ defects (by promotion of electrons into the conduction band), which could be present in the material, we find again large vertical ionization energies (close to 6 eV), whereas adiabatic energies are in the range 4.1-4.3 eV, also close to the experimental threshold energy for the observation of photocatalysis.

All the above transitions induce quite large changes to the local P-O bonding. That would explain the XPS and FTIR experiments of Refs. 38, 30 and 32, that show a clear transformation of the P-O bonds upon UV illumination of HAp. However, based on our results it is not possible to provide a final assignment to that effect. Decisive help would be provided by combining local vibrational mode calculations with vibrational FTIR spectroscopy on samples with good quality. Despite the uncertainty, our results suggest that the excitation channel (ii), which involves a photo-induced bond-breaking of extended structures, and shows a transition energy in excellent agreement with the observations, appears to be the strongest candidate to explain the onset absorption of HAp in the range 3.4-4.0 eV.

Conclusions

We presented a study of the structural and electronic properties of oxygen vacancies in hydroxyapatite by means of hybrid density functional theory within the plane-wave formalism. The vacancies were investigated in large supercells, from which formation energies and electronic transition energies were calculated.

We found that the vacancies essentially occur in two distinct forms, either as a simple vacant oxygen site (referred to as structures I-IV), or as an oxygen atom replacing two neighboring oxygen vacancies (extended structures A-C). The former type of vacancies are deep donors, while the latter are shallow donors with rather low ionization energies. No acceptor states (stable negatively charged defects) were found.

Vacancy structures I-IV are more stable in the neutral charge state, while extended structures A-C are preferred in the double plus charge state. This means that the oxygen vacancy adopts rather different configurations on samples where the Fermi energy is in the upper or the lower half of the band gap. The large relaxation energies upon ionization makes the oxygen vacancy a negative- U defect, where the single plus charge state is metastable, being only attainable under excitation (for instance by UV illumination).

From inspection of the one-electron Kohn-Sham levels, combined with the transition levels obtained from total energies, we find that electron promotion from the valence band top to the donor state of the positively charged structures, involves a zero-phonon absorption of 3.6-3.9 eV. This transition leads to a spontaneous breaking of either P-O-P or O-H-O bridge-bonds, and most likely explains the 3.4-4.0 eV absorption onset for the observation of photocatalysis under persistent UV illumination.

Acknowledgement This work was supported by the *Fundação para a Ciência e a Tecnologia* (FCT) through project UID/CTM/50025/2013 and by the Russian Foundation for Basic Research (RFBR) through Grant No. 19-01-00519 A.

References

- (1) Kay, M. I.; Young, R. A.; Posner, A. S. Crystal structure of hydroxyapatite. *Nature* **1964**, *204*, 1050.
- (2) Young, R. A. Dependence of apatite properties on crystal structural details. *Transactions of the New York Academy of Sciences* **1967**, *29*, 949.
- (3) Elliot, J. C. *Studies in Inorganic Chemistry*, 1st ed.; Elsevier: Amsterdam, 1994; Vol. 18.
- (4) Currey, J. D. *Bones - Structures and Mechanics*, 2nd ed.; Princeton University Press: Princeton, New Jersey, 2002.
- (5) Koester, K. J.; Ager III, J. W.; Ritchie, R. O. The true toughness of human cortical bone measured with realistically short cracks. *Nature Materials* **2008**, *7*, 672-677.
- (6) Weiner, S.; Price, P. A. Disaggregation of bone into crystals. *Calcified Tissue International* **1986**, *39*, 365-375.
- (7) Kanzaki, N.; Onuma, K.; Ito, A.; Teraoka, K.; Tateishi, T.; Tsutsumi, S. Direct growth rate measurement of hydroxyapatite single crystal by moire phase shift interferometry. *The Journal of Physical Chemistry B* **1998**, *102*, 6471-6476.
- (8) Bystrov, V. S.; Paramonova, E.; Dekhtyar, Y.; Katashev, A.; Karlov, A.; Polyaka, N.; Bystrova, A. V.; Patmalnieks, A.; Kholkin, A. L. Computational and experimental studies of size and shape related physical properties of hydroxyapatite nanoparticles. *Journal of Physics: Condensed Matter* **2011**, *23*, 065302.
- (9) Ratner, B. D.; Hoffman, A. S.; Schoen, F. J.; Lemons, J. E. *Biomaterials Science*, third edition ed.; Academic Press: Oxford, 2013.
- (10) Best, S. M.; Porter, A. E.; Thian, E. S.; Huang, J. *Bioceramics: Past, present and*

- for the future. *Journal of the European Ceramic Society* **2008**, *28*, 1319–1327.
- (11) Leon, B.; Janson, J. A. *Thin calcium phosphate coatings for medical implants*; Springer-Verlag: New York, 2009.
 - (12) Kobayashi, T.; Nakamura, S.; Yamashita, K. Enhanced osteobonding by negative surface charges of electrically polarized hydroxyapatite. *Journal of Biomedical Materials Research* **2001**, *57*, 477–484.
 - (13) Nakamura, M.; Nagai, A.; Tanaka, Y.; Sekijima, Y.; Yamashita, K. Polarized hydroxyapatite promotes spread and motility of osteoblastic cells. *Journal of Biomedical Materials Research Part A* **2009**, *92A*, 783–790.
 - (14) Slepko, A.; Demkov, A. A. First principles study of hydroxyapatite surface. *The Journal of Chemical Physics* **2013**, *139*, 044714.
 - (15) Zeglinski, J.; Nolan, M.; Thompson, D.; Tofail, S. A. M. Reassigning the most stable surface of hydroxyapatite to the water resistant hydroxyl terminated (010) surface. *Surface Science* **2014**, *623*, 55–63.
 - (16) Nakamura, S.; Takeda, H.; Yamashita, K. Proton transport polarization and depolarization of hydroxyapatite ceramics. *Journal of Applied Physics* **2001**, *89*, 5386–5392.
 - (17) Bystrov, V. S.; Bystrova, N. K.; Paramonova, E. V.; Dekhtyar, Y. D. Interaction of charged hydroxyapatite and living cells. I. Hydroxyapatite polarization properties. *Mathematical biology and Bioinformatics* **2009**, *4*, 7–11.
 - (18) Horiuchi, N.; Nakamura, M.; Nagai, A.; Katayama, K.; Yamashita, K. Proton conduction related electrical dipole and space charge polarization in hydroxyapatite. *Journal of Applied Physics* **2012**, *112*, 074901.
 - (19) Tofail, S. A. M.; Haverty, D.; Stanton, K. T.; McMonagle, J. B. Structural order and dielectric behaviour of hydroxyapatite. *Ferroelectrics* **2005**, *319*, 117–123.
 - (20) Hitmi, N.; LaCabanne, C.; Bonel, G.; Roux, P.; Young, R. A. Dipole cooperative motions in an A-type carbonated apatite, $\text{Sr}_10(\text{AsO}_4)_6\text{CO}_3$. *Journal of Physics and Chemistry of Solids* **1986**, *47*, 507–515.
 - (21) Hitmi, N.; LaCabanne, C.; Young, R. A. OH-reorientability in hydroxyapatites: effect of F- and Cl-. *Journal of Physics and Chemistry of Solids* **1988**, *49*, 541–550.
 - (22) Lang, S. B.; Tofail, S. A. M.; Gandhi, A. A.; Gregor, M.; Wolf-Brandstetter, C.; Kost, J.; Bauer, S.; Krause, M. Pyroelectric, piezoelectric, and photoeffects in hydroxyapatite thin films on silicon. *Applied Physics Letters* **2011**, *98*, 123703.
 - (23) Lang, S. B.; Tofail, S. A. M.; Kholkin, A. L.; Wojtaś, M.; Gregor, M.; Gandhi, A. A.; Wang, Y.; Bauer, S.; Krause, M.; Plecenik, A. Ferroelectric polarization in nanocrystalline hydroxyapatite thin films on silicon. *Scientific Reports* **2013**, *3*, 2215.
 - (24) Lang, S. B. Review of ferroelectric hydroxyapatite and its application to biomedicine. *Phase Transitions* **2016**, *89*, 678–694.
 - (25) Tofail, S. A. M.; Gandhi, A. A.; Gregor, M.; Bauer, J. Electrical properties of hydroxyapatite. *Pure and Applied Chemistry* **2015**, *87*, 221–229.
 - (26) Tofail, S. A. M.; Bauer, J. *Electrically active materials for medical devices*; IMPERIAL COLLEGE PRESS, 2016.
 - (27) Nishikawa, H.; Omamiuda, K. Photocatalytic activity of hydroxyapatite for methyl mercaptane. *Journal of Molecular*

- Catalysis A: Chemical* **2002**, *179*, 193–200.
- (28) Nishikawa, H. A high active type of hydroxyapatite for photocatalytic decomposition of dimethyl sulfide under UV irradiation. *Journal of Molecular Catalysis A: Chemical* **2004**, *207*, 149–153.
- (29) Ozeki, K.; Janurudin, J. M.; Aoki, H.; Fukui, Y. Photocatalytic hydroxyapatite/titanium dioxide multilayer thin film deposited onto glass using an rf magnetron sputtering technique. *Applied Surface Science* **2007**, *253*, 3397–3401.
- (30) Reddy, M. P.; Venugopal, A.; Subrahmanyam, M. Hydroxyapatite photocatalytic degradation of calmagite (an azo dye) in aqueous suspension. *Applied Catalysis B: Environmental* **2007**, *69*, 164–170.
- (31) Tsukada, M.; Wakamura, M.; Yoshida, N.; Watanabe, T. Band gap and photocatalytic properties of Ti-substituted hydroxyapatite: comparison with anatase-TiO₂. *Journal of Molecular Catalysis A: Chemical* **2011**, *338*, 18–23.
- (32) Shariffuddin, J. H.; Jones, M. I.; Patterson, D. A. Greener photocatalysts: Hydroxyapatite derived from waste mussel shells for the photocatalytic degradation of a model azo dye wastewater. *Chemical Engineering Research and Design* **2013**, *91*, 1693–1704.
- (33) Brazón, E. M.; Piccirillo, C.; Moreira, I.; Castro, P. Photodegradation of pharmaceutical persistent pollutants using hydroxyapatite-based materials. *Journal of Environmental Management* **2016**, *182*, 486–495.
- (34) Piccirillo, C.; Castro, P. L. Calcium hydroxyapatite-based photocatalysts for environment remediation: characteristics, performances and future perspectives. *Journal of Environmental Management* **2017**, *193*, 79–91.
- (35) Wakamura, M.; Hashimoto, K.; Watanabe, T. Photocatalysis by calcium hydroxyapatite modified with Ti(IV): albumin decomposition and bactericidal effect. *Langmuir* **2003**, *19*, 3428–3431.
- (36) Hu, A.; Li, M.; Chang, C.; Mao, D. Preparation and characterization of a titanium-substituted hydroxyapatite photocatalyst. *Journal of Molecular Catalysis A: Chemical* **2007**, *267*, 79–85.
- (37) Xu, J.; Xu, P.; Li, Z.; Huang, J.; Yang, Z. Oxidative stress and apoptosis induced by hydroxyapatite nanoparticles in C6 cells. *Journal of Biomedical Materials Research Part A* **2011**, *100A*, 738–745.
- (38) Nishikawa, H. Photo-induced catalytic activity of hydroxyapatite based on photo-excitation. *Phosphorus Research Bulletin* **2007**, *21*, 97–102.
- (39) Nishikawa, H. Radical generation on hydroxyapatite by UV irradiation. *Materials Letters* **2003**, *58*, 14–16.
- (40) Bystrov, V. S.; Coutinho, J.; Bystrova, A. V.; Dekhtyar, Y. D.; Pullar, R. C.; Poronin, A.; Palcevskis, E.; Dindune, A.; Alkan, B.; Durucan, C.; Paramonova, E. V. Computational study of hydroxyapatite structures, properties and defects. *Journal of Physics D: Applied Physics* **2015**, *48*, 195302.
- (41) Bystrov, V. S.; Piccirillo, C.; Tobaldi, D. M.; Castro, P. M. L.; Coutinho, J.; Kopyl, S.; Pullar, R. C. Oxygen vacancies, the optical band gap (E_g) and photocatalysis of hydroxyapatite: comparing modelling with measured data. *Applied Catalysis B: Environmental* **2016**, *196*, 100–107.
- (42) Martin, R. M.; Reining, L.; Ceperley, D. M. *Interacting Electrons: Theory and Computational Approaches*; Cambridge University Press: Cambridge, 2016.
- (43) Avakyan, L. A.; Paramonova, E. V.; Coutinho, J.; Öberg, S.; Bystrov, V. S.;

- Bugaev, L. A. Optoelectronics and defect levels in hydroxyapatite by first-principles. *The Journal of Chemical Physics* **2018**, *148*, 154706.
- (44) Calderin, L.; Stott, M. J.; Rubio, A. Electronic and crystallographic structure of apatites. *Phys. Rev. B* **2003**, *67*, 134106.
- (45) Rulis, P.; Ouyang, L.; Ching, W. Y. Electronic structure and bonding in calcium apatite crystals: Hydroxyapatite, fluorapatite, chlorapatite, and bromapatite. *Physical Review B* **2004**, *70*, 155104.
- (46) Rulis, P.; Yao, H.; Ouyang, L.; Ching, W. Y. Electronic structure, bonding, charge distribution, and x-ray absorption spectra of the (001) surfaces of fluorapatite and hydroxyapatite from first principles. *Physical Review B* **2007**, *76*, 245410.
- (47) Matsunaga, K.; Kuwabara, A. First-principles study of vacancy formation in hydroxyapatite. *Physical Review B* **2007**, *75*, 014102.
- (48) Slepko, A.; Demkov, A. A. First-principles study of the biomineral hydroxyapatite. *Physical Review B* **2011**, *84*, 134108.
- (49) Rosenman, G.; Aronov, D.; Oster, L.; Haddad, J.; Mezinskas, G.; Pavlovska, I.; Chaikina, M.; Karlov, A. Photoluminescence and surface photovoltage spectroscopy studies of hydroxyapatite nanobio-ceramics. *Journal of Luminescence* **2007**, *122-123*, 936–938.
- (50) Kresse, G.; Hafner, J. Ab initio. *Physical Review B* **1994**, *49*, 14251–14269.
- (51) Kresse, G.; Furthmüller, J. Efficient iterative schemes for ab initio total-energy calculations using a plane-wave basis set. *Physical Review B* **1996**, *54*, 11169–11186.
- (52) Kresse, G.; Joubert, D. From ultrasoft pseudopotentials to the projector augmented-wave method. *Physical Review B* **1999**, *59*, 1758–1775.
- (53) Perdew, J. P.; Burke, K.; Ernzerhof, M. Generalized Gradient Approximation Made Simple. *Physical Review Letters* **1996**, *77*, 3865–3868.
- (54) Lee, C.; Yang, W.; Parr, R. G. Development of the Colle-Salvetti correlation-energy formula into a functional of the electron density. *Physical Review B* **1988**, *37*, 785–789.
- (55) Becke, A. D. A new mixing of Hartree-Fock and local density-functional theories. *The Journal of Chemical Physics* **1993**, *98*, 1372–1377.
- (56) Blöchl, P. E. Projector augmented-wave method. *Physical Review B* **1994**, *50*, 17953–17979.
- (57) Haverty, D.; Tofail, S. A. M.; Stanton, K. T.; McMonagle, J. B. Structure and stability of hydroxyapatite: density functional calculation and Rietveld analysis. *Physical Review B* **2005**, *71*.
- (58) Ma, G.; Liu, X. Y. Hydroxyapatite: hexagonal or monoclinic? *Crystal Growth & Design* **2009**, *9*, 2991–2994.
- (59) Hughes, J. M.; Cameron, M.; Crowley, K. D. Structural variations in natural F, OH, and Cl apatites. *American Mineralogist* **1989**, *74*, 870–876.
- (60) Coutinho, J.; Torres, V. J. B.; Demmouche, K.; Öberg, S. Theory of the carbon vacancy in 4H -SiC: Crystal field and pseudo-Jahn-Teller effects. *Physical Review B* **2017**, *96*.
- (61) Gouveia, J. D.; Coutinho, J. Can we rely on hybrid-DFT energies of solid-state problems with local-DFT geometries. *Electronic Structure (to appear in)* **2019**,
- (62) Qian, G.-X.; Martin, R. M.; Chadi, D. J. First-principles study of the atomic reconstructions and energies of Ga- and As-stabilized GaAs(100) surfaces. *Physical Review B* **1988**, *38*, 7649–7663.

- (63) Makov, G.; Payne, M. C. Periodic boundary conditions in ab initio calculations. *Physical Review B* **1995**, *51*, 4014–4022.
- (64) Freysoldt, C.; Neugebauer, J.; Van de Walle, C. G. Fully Ab Initio Finite-Size Corrections for Charged-Defect Supercell Calculations. *Physical Review Letters* **2009**, *102*, 016402.
- (65) Kumagai, Y.; Oba, F. Electrostatics-based finite-size corrections for first-principles point defect calculations. *Physical Review B* **2014**, *89*, 195205.
- (66) Koopmans, T. Über die Zuordnung von Wellenfunktionen und Eigenwerten zu den Einzelnen Elektronen Eines Atoms. *Physica* **1934**, *1*, 104–113.
- (67) Perdew, J. P.; Parr, R. G.; Levy, M.; Balduz, J. L. Density-functional theory for fractional particle number: derivative discontinuities of the energy. *Physical Review Letters* **1982**, *49*, 1691–1694.
- (68) Anderson, P. W. Model for the electronic structure of amorphous semiconductors. *Physical Review Letters* **1975**, *34*, 953–955.
- (69) Watkins, G. D. In *Festkörperprobleme 24*; Grosse, P., Ed.; Advances in Solid State Physics; Springer-Verlag: Berlin, Heidelberg, 1984; Vol. 24; Chapter Negative- U properties for defects in solids, pp 163–189.

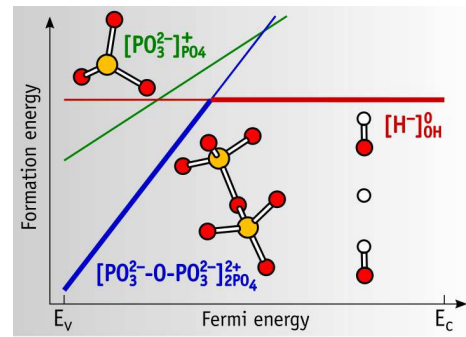


Table of Contents Graphic